13th International Symposium on Turbulence and Shear Flow Phenomena (TSFP13)
Montreal, Canada, June 25-28, 2024

SPECTRAL POD ANALYSIS OF THE AHMED BODY WAKE AT HIGH REYNOLDS NUMBERS

Robert J.G. Forgie
Department of Mechanical Engineering
University of Alberta
Edmonton, Alberta, T6G 2R3, Canada
rforgie@ualberta.ca

Kareem Ali
Department of Mechanical Engineering
University of Alberta
Edmonton, Alberta, T6G 2R3, Canada
kareem1@ualberta.ca

Sen Wang
Department of Mechanical Engineering
University of Alberta
Edmonton, Alberta, T6G 2R3, Canada
sen6@ualberta.ca

Sina Ghaemi
Department of Mechanical Engineering
University of Alberta
Edmonton, Alberta, T6G 2R3, Canada
ghaemi@ualberta.ca

ABSTRACT

This paper presents an experimental investigation into coherent motions observed in the near wake of the Ahmed body geometry at high Reynolds numbers. The investigation started by analyzing a 2D section of the 3D tomographic particle image velocimetry (tomo-PIV) dataset provided by Chen et al. (2024) at Reynolds numbers *Re* of 10,000 to evaluate the feasibility of identifying similar coherent motions from 2D measurements. Following this evaluation, new time-resolved stereoscopic PIV (stereo-PIV) data was acquired within the crossflow plane of the wake flow at higher *Re* values of 46,400, 139,000, and 232,000. Spectral proper orthogonal decomposition (SPOD) was then applied to these time-resolved 2D measurements. Using these SPOD modes, the dynamics of the flow motions at different frequencies are reconstructed. The results include the barycentre trace for the full phase of the motion and reconstructions of the flow velocity at each frequency range. Interpretation of the reconstructed flow dynamics show distinct counter-rotating vortices and bi-stable motion for Strouhal number $St < 0.016$. Two smaller counter-rotating vortices and a smaller spanwise travel of the barycentre are attributed to a spanwise flapping motion within the range of $0.016 \leq St < 0.051$. A vertical barycentre trace and spanwise-symmetric behaviour of the wake indicate a vertical flapping motion for $0.051 \leq St < 0.110$. Vortex shedding in both spanwise and wall-normal directions is observed in the range of $0.110 \leq St < 0.250$, and small-scale turbulent structures are observed for $0.250 < St \leq 1.000$. Contrary to results from Chen et al. (2024) at lower *Re*, spanwise and vertical flapping motions were found at distinct *St* ranges.

INTRODUCTION

The Ahmed body is a 3D bluff geometry resembling a simplified road vehicle with a large recirculation region (Ahmed et al., 1984). The early investigations of Duell and George (1999) and Khalighi et al. (2001) observed a vortex-shedding process, as well as a pumping motion corresponding to periodic streamwise movements of the stagnation point. More recently, Grandemange et. al (2013) showed a switching phenomenon of the spanwise position of the recirculation bubble between two low-energy states, referred to as bi-stability. In addition, high-frequency instabilities of the shear layer were also observed by Haffner et al. (2020).

In a recent investigation by Chen et al. (2024), the motions in the wake of the Ahmed body were reconstructed using time-resolved tomographic particle image velocimetry (tomo-PIV) measurements in a water flume. SPOD was applied and four distinct flow motions were found in the wake of the Ahmed body. However, the measurements of Chen et al. (2024) were limited to $Re = 10{,}000$ due to complications of capturing time-resolved tomo-PIV measurement for larger models and in a wind tunnel with higher *Re* values. Therefore, it is desirable to investigate if a 2D crossflow measurement using stereo-PIV is sufficient to identify the same flow motions at the same *Re*. Once this is evaluated and limitations are identified, it is possible to utilize time-resolved stereo-PIV measurements in a wind tunnel to extend the analysis to wake flows at higher *Re*.

EXPERIMENTAL METHODOLOGY

The experiments were carried out in a large two-story, closed-loop wind tunnel at the University of Alberta. The wind-tunnel nozzle has a contraction ratio of 6.3:1, and the test section has a cross-section of 1.2×2.4 m^2. The experiments were conducted at free-stream velocities of $U_\infty = 5$, 15, and 25 m/s, corresponding to Reynolds numbers of $Re = 46{,}400$, 139,000, and 232,000, respectively. Here, $Re = U_\infty H/\nu$, where H is the Ahmed body height and ν is the kinematic viscosity of air.

An Ahmed body with height $H = 144$ mm was mounted on a flat plate as seen in Figure 1. The flat plate had a length of 1.15 m and a width of 0.80 m. It featured an optimized leading edge (LE) profile and a tapered trailing edge (Hanson et al., 2012). The Ahmed body was positioned along the spanwise centre of the tunnel and elevated 25 mm above the flat plate, which was elevated 110 mm above the tunnel floor. The LE of the Ahmed body was located 200 mm downstream of the flat plate LE.

The stereo-PIV setup was comprised of two high-speed cameras (Phantom, V611) with an angle of 90°. Scheimpflug adapters were installed to maximize this angle and thereby minimize image distortion (Prasad and Jensen, 1995). The cameras were equipped with Nikon lenses with a focal length of $f = 200$ mm and an aperture size of $f/16$. The cameras imaged at a resolution of about 0.19 mm per pixel, resulting in a field of view of 201×159 mm^2. A dual-cavity high-speed Nd:YLF laser (Photonics Industries, DM20-527DH) was used in combination with spherical and cylindrical lenses to form a spanwise-wall-normal laser sheet with an average thickness of 2.3 mm. The laser sheet was located 1.1H downstream of the Ahmed body. The air flow was seeded using 1 μm droplets dispersed by a fog generator (Fog Fury 3000). For each Reynolds number, 10 sets

of 3900 double-frame time-resolved images were collected at frequencies f = 87, 261, and 435 Hz, for Re = 46,400, 139,000, and 232,000, respectively. A three-dimensional calibration target (Type 22, LaVision GmbH) was used for camera calibration. The calibration image was mapped using a third-order polynomial in Davis 8.4 (LaVision GmbH). The final root-mean-square (RMS) values of the calibration polynomial fit were 0.11 and 0.52 pixels for cameras 1 and 2, respectively.

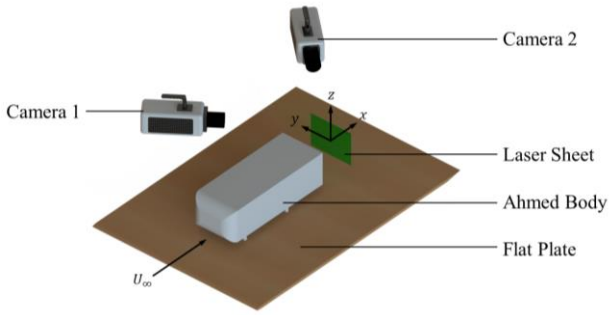

Figure 1. The stereoscopic PIV experimental setup.

The coordinate system is presented in Figure 1 with x, y, and z corresponding to streamwise, spanwise, and wall-normal directions. U, V, and W are the velocity components in the x, y, and z directions while u, v, and w are the fluctuating components, respectively. Vector fields were obtained with stereoscopic cross-correlation using a multi-pass algorithm with a final interrogation window of 32×32 pixel (6.15×6.15 mm^2) at 75% overlap (DaVis 8.4, LaVision GmbH). Spurious vectors were removed using universal outlier detection and replaced by interpolated vectors (Westerweel and Scarano, 2005). The velocity vectors were then cropped to the width and height of the Ahmed body to remove noisy borders.

An additional challenge is achieving spanwise symmetry of time-averaged velocity fields for SPOD given the short duration of the measurement and large periods of bi-stability asymmetric motion. To address this, spanwise symmetry was enforced by copying the datasets, flipping the velocities in the spanwise direction, and reversing the spanwise velocities. These copied datasets were then appended to the original datasets prior to processing (Podvin et al., 2020).

SPOD was performed as presented by Towne et al. (2018). Using MATLAB (MathWorks), 20 time-resolved stereo-PIV datasets (10 original and 10 flipped datasets) were each divided into 6 segments with 50% overlap. A Hamming window was applied, and then the fast Fourier transform (FFT) algorithm was used to transform the data into the frequency domain. The cross-spectral density was then calculated using the method of snapshots (Sirovich, 1987). Subsequently, the eigenvalues λ and eigenvectors (SPOD modes) Ψ_l were calculated at each frequency index l.

A reduced order model (ROM) was constructed using the SPOD modes at various frequencies as per the procedure outlined in Nekkanti & Schmidt (2021). The ROM of the streamwise component of velocity U_{ROM} at a given frequency f_l and phase ϕ is given by:

$$U_{\mathrm{ROM}} = \langle U \rangle / U_\infty + \mathcal{R}e\left(\Psi_{u,l}/U_\infty \times \mathrm{e}^{i\phi}\right) \quad (1)$$

where $\mathcal{R}e$ is the real part of a complex number, $\Psi_{u,l}$ is the streamwise component of Ψ_l, and $\langle U \rangle$ is the time-averaged streamwise velocity. Similar equations were used to reconstruct the spanwise and wall-normal ROM of velocities. The reconstructed u_{ROM} using the velocity fluctuations is defined using:

$$u_{\mathrm{ROM}} = \mathcal{R}e\left(\Psi_{u,l}/U_\infty \times \mathrm{e}^{i\phi}\right) \quad (2)$$

The duration of each ROM cycle is equal to $1/f_l$. Additionally, ROMs were used to calculate the barycentre of momentum deficit, a marker of the position of the wake. The barycentre y_b coordinate is calculated using:

$$y_b = \frac{\iint_A y(1-U_{\mathrm{ROM}})dA}{\iint_A (1-U_{\mathrm{ROM}})dA} \quad (3)$$

The integrals are calculated within the wake area A defined as $U_{\mathrm{ROM}} < 1$. The z-coordinate of the barycentre z_b is calculated in a similar manner. Together, the energy distribution from the premultiplied spectra, the trace of the ROM barycentre of momentum deficit, and the ROM velocity reconstructions helped identify and characterize the flow motions.

EVALUATION OF SPOD IN CROSSFLOW PLANE

A 2D crossflow slice of the tomo-PIV data collected by Chen et al. (2024) was selected for SPOD analysis. The streamwise position of the slice was selected based on the average streamwise position of the barycentre, found to be ~1.1H downstream of the base of the model in the analysis of Chen et al. (2024). The premultiplied spectra of first SPOD mode for the 3D data and the 2D crossflow plane are presented in Figure 2(a) as a function of Strouhal number, $St = fH/U_\infty$. The results show that both spectra exhibit a similar energy distribution, while the 2D crossflow slice displays a notably smaller magnitude. The latter is attributed to the smaller kinetic energy of the 2D slice compared to the kinetic energy of the larger volumetric measurement. Chen et al. (2024) investigated the flow dynamics associated with different St, and categorized the flow motions corresponding to zones A, B, C, D, and E of Figure 2(a) to bi-stability, swinging/flapping, vortex shedding, small-scale structures, and shear-layer instability, respectively.

Using the SPOD modes, a reduced order model (ROM) was created to obtain the position of the wake barycentre for a sample St case. The trace of the barycentre is plotted in Figure 2(b) for St = 0.007 for the 3D and 2D ROM reconstructions from Chen et al. (2024). The traces show similar shape, with the 2D trace showing greater spanwise travel and a smaller wall-normal offset. The similarity of both the premultiplied spectra and the barycentre trace suggest that the 2D crossflow measurement can be used for capturing dynamics of the wake although the information will be limited to a crossflow plane. This observation allows the relaxation of the measurement requirement from 3D tomo-PIV to 2D stereo-PIV in a crossflow plane of the wake.

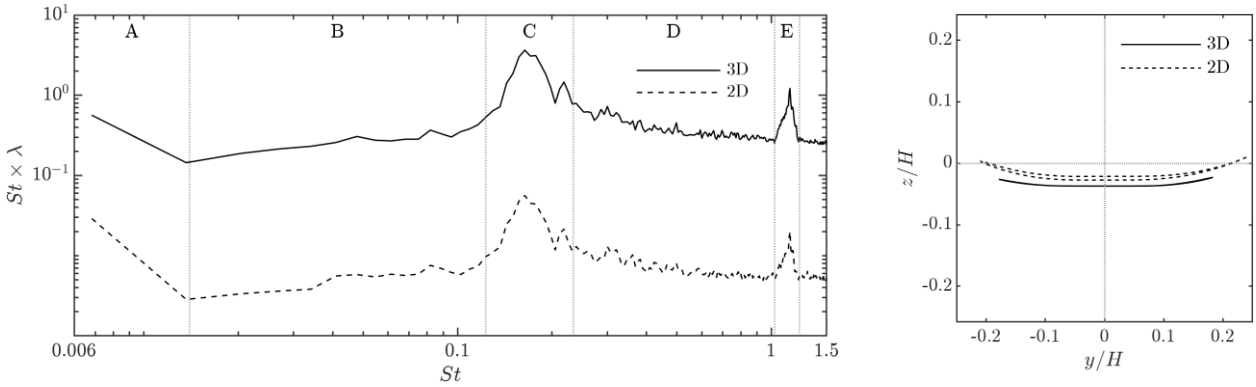

(a) (b)

Figure 2. (a) Comparison between premultiplied spectra for the 3D tomographic data and a 2D slice of the data (Chen et al., 2024) and (b) Comparison between barycentre traces at St = 0.007 for the 3D tomographic data and a 2D slice of the data (Chen et al., 2024).

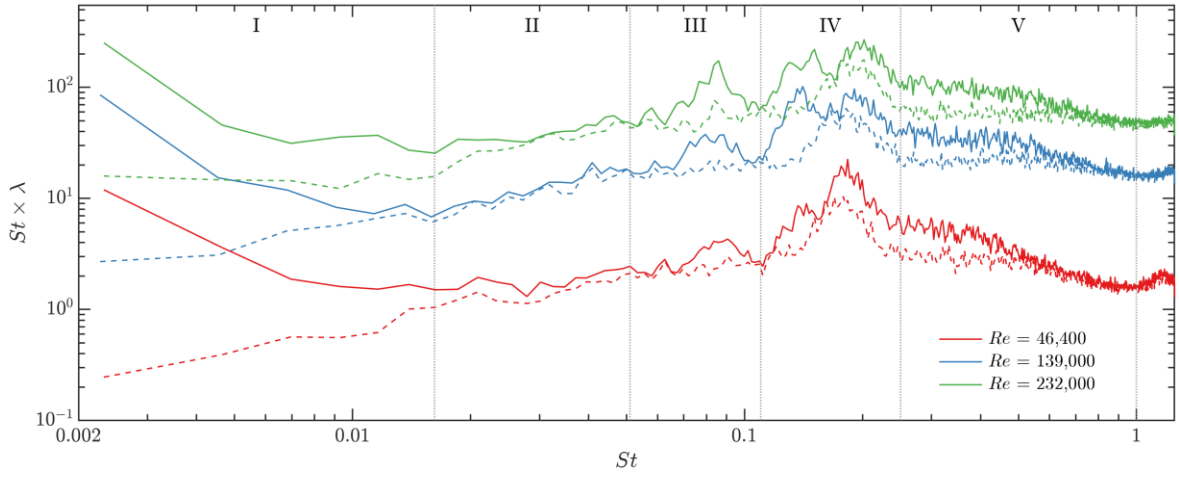

Figure 3. Premultiplied spectra for the three Re of interest. Solid lines show the first SPOD mode, while dotted lines show the second SPOD mode.

HIGH REYNOLDS NUMBERS

The stereo-PIV measurements at Re = 46,400, 139,000, and 232,000 were analysed using SPOD. The premultiplied spectra of the first and second SPOD modes are shown in Figure 3. Overall, the spectra look similar for the first mode; starting with a high energy at the lowest resolved St, then a reduction in the energy, followed by an energy increase to reach successive local peak values before a final decline in energy. The second mode shows a smaller magnitude of energy than the first mode at low St but similar energy beyond St = 0.02, except at the peaks of the first mode where the discrepancy in energy is larger between the two modes. Between the three Re cases, the energy trends are similar, except that there are less pronounced peaks in the first mode at St = 0.085 and 0.15 for the lowest Re case. Five distinct zones were classified in the premultiplied spectra based on spatial and temporal characteristics of the flow motions described by the first two modes within each zone. These zones are summarized in Table 1 and are discussed in detail in the subsequent sections.

Table 1. The flow motions and St range of each zone presented in Figure 3.

Zone	Flow Motion	St
I	Bi-stability	$St < 0.016$
II	Spanwise flapping motions	$0.016 \leq St < 0.051$
III	Vertical flapping motions	$0.051 \leq St < 0.110$
IV	Vortex shedding	$0.110 \leq St < 0.250$
V	Small-scale structures	$0.250 \leq St < 1.000$

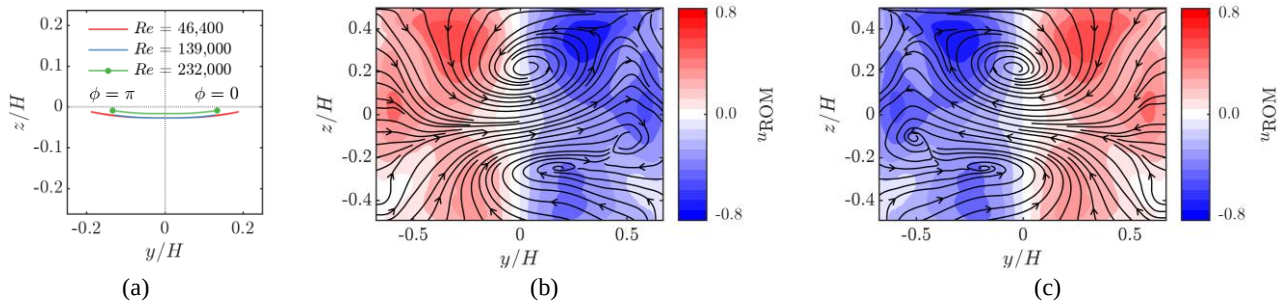

Figure 4. (a) Barycentre trace for all three *Re* at *St* = 0.005 showing bi-stability, (b) ROM reconstruction for the rightmost barycentre location at *Re* = 232,000, (c) ROM reconstruction for the leftmost barycentre location at *Re* = 232,000.

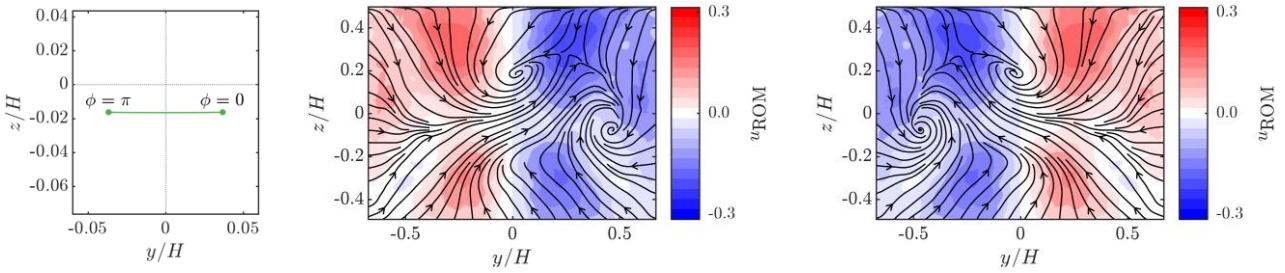

Figure 5. (a) Barycentre trace for *Re* = 232,000 at *St* = 0.042 showing spanwise flapping motions, and ROM reconstructions at *Re* = 232,000 for the (b) rightmost barycentre location for the first SPOD mode and the (c) leftmost barycentre location for the first SPOD mode.

Bi-stability

This section discusses the SPOD modes for *St* < 0.016, represented in Figure 3 as zone I. This zone is characterized by a large energy drop-off in the first mode as *St* increases. Also, the first mode has a much higher energy than the second mode. Figure 4(a) shows a trace of the barycentre of momentum deficit for the ROM for *St* = 0.005 of the first SPOD mode. The three *Re* show symmetric spanwise oscillation with small wall-normal displacements, resembling a shallow arc. The traces are closed-loop paths over the phase ϕ = 0 to 2π but appear as single lines as they retrace their own paths. The trace is consistent with the movement of the wake between two spanwise positions in bi-stable switching. The lowest *Re* case has the greatest spanwise displacement, ranging from *y/H* = -0.19 to 0.19, with the two higher *Re* cases both having displacements of *y/H* = -0.13 to 0.13. The two lowest *Re* cases appear to be overlayed with nearly identical paths whereas the highest *Re* case has a constant vertical offset of z/*H* = 0.01 throughout the trajectory of the motion.

The ROM reconstructions in Figures 4(b) and 4(c) correspond to the leftmost and rightmost locations of the barycentre, respectively, at *Re* = 232,000. Characteristic of this motion seen from the streamlines are two counter-rotating vortices: a strong vortex close to the top of the Ahmed body, and a weaker vortex below it. These vortices cause a spanwise motion towards the side opposite to the barycentre location. Additionally, the ROM of the streamwise velocity is antisymmetric about *y/H* = 0. When the barycentre is at the spanwise centre of the Ahmed body, a symmetric state can be observed as the bi-stable switching takes place at $\phi = \pi/2$ and $3\pi/2$. These characteristics are consistent with observations of bi-stability in stereo-PIV measurements by Pavia et al. (2018), and the 3D observations of bi-stability by Chen et al. (2024).

Spanwise Flapping Motions

This section discusses the SPOD modes in the range of 0.016 ≤ *St* < 0.051. This range is referred to as zone II in Figure 3 and is characterized by similar energy magnitude between the first and second SPOD modes. Figure 5(a) shows a trace of the barycentre at *St* = 0.046 for the first SPOD mode of the *Re* = 232,000 case. The trace resembles a horizontal line at *z/H* = -0.017 with spanwise travel from *y/H* = -0.04 to 0.04. This is similar to Figure 4(a) but with a significantly smaller span and no curvature of the trajectory, suggesting a much weaker spanwise oscillation of the wake. This behaviour is consistent throughout zone B, with the spanwise travel of the barycentre gradually decreasing as *St* increases.

The mode reconstructions in Figures 5(b) and 5(c) represent the first SPOD mode at *St* = 0.046 and phase angles $\phi = 0$ and π. The u_{ROM} contours show an antisymmetric pattern about *y/H* = 0 with a notably smaller magnitude than in zone I. The streamlines indicate two streamwise vortices located at [*y/H, z/H*] = [0.48, -0.10] and [0.01, 0.18], overlaying the negative u_{ROM} contours.

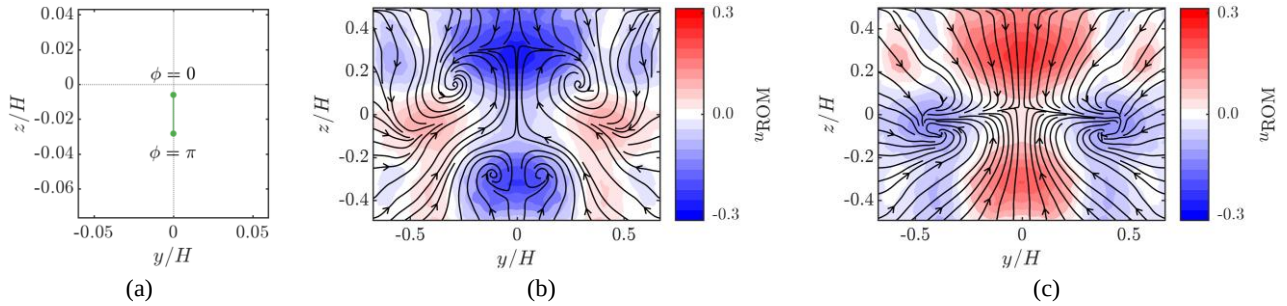

Figure 6. (a) Barycentre trace for Re = 232,000 at St = 0.088 showing flapping motions, and ROM reconstructions at Re = 232,000 for the (b) topmost barycentre location for the first SPOD mode, (c) bottommost barycentre location for the first SPOD mode.

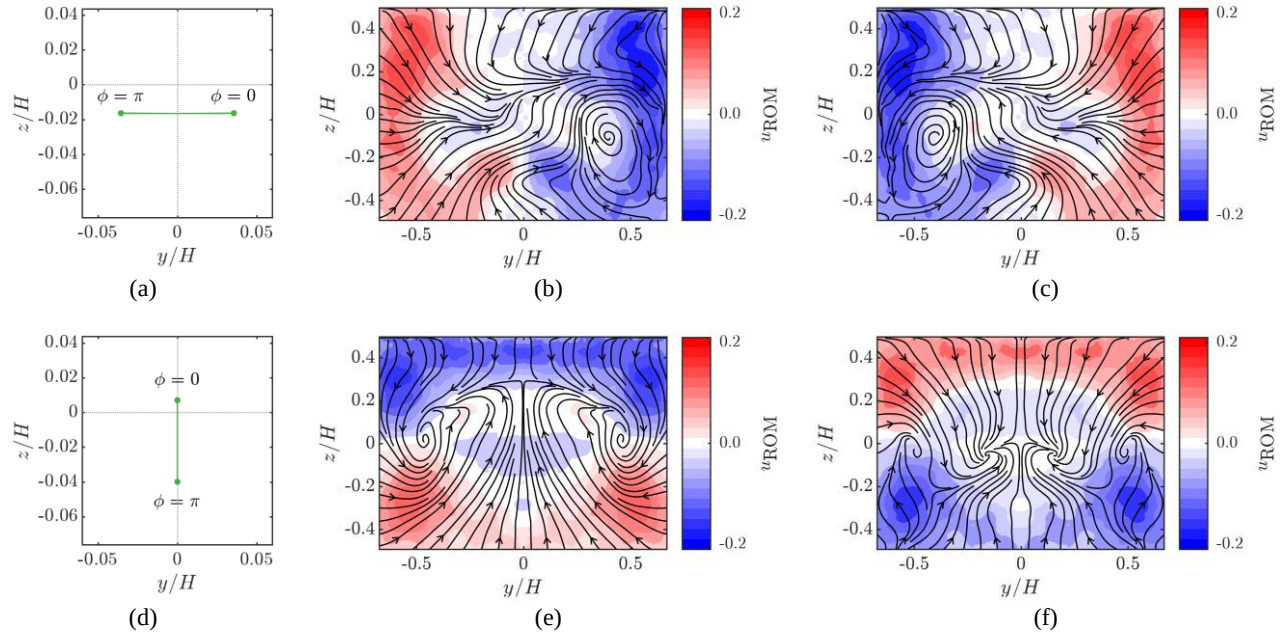

Figure 7. (a) Barycentre trace for Re = 232,000 at St = 0.149 showing spanwise vortex shedding, and ROM reconstructions at Re = 232,000 for the (b) rightmost barycentre location for the first SPOD mode, (c) leftmost barycentre location for the second SPOD mode. (d) Barycentre trace for Re = 232,000 at St = 0.197 showing spanwise vortex shedding, and ROM reconstructions at Re = 232,000 for the (e) rightmost barycentre location for the first SPOD mode, (f) leftmost barycentre location for the second SPOD mode.

As the phase angle increases from $\phi = 0$ to $\pi/2$, the vortices move in the negative spanwise direction, disappearing at the spanwise center line. From $\phi = \pi/2$ to π, the u_{ROM} contours flip about y/H = 0 and the streamwise vortices reappear at [y/H, z/H] = [-0.48, -0.1] and [0.01, 0.18].

Throughout zone II, the first SPOD mode consistently shows the antisymmetric u_{ROM} contours with two streamwise vortices and small spanwise movement of the barycentre. In zone III, the spanwise flapping motions appear as the second SPOD mode.

Vertical Flapping Motions

This section discusses the SPOD modes in the range of 0.051 $\leq St <$ 0.102, or zone III in Figure 3, where the first SPOD mode shows a peak in energy. Figure 6(a) shows a trace of the barycentre at St = 0.088 for the first SPOD mode of the Re = 232,000 case. The figure shows a vertical line at y/H = 0 with wall-normal travel from z/H = -0.029 to -0.005. The mode reconstruction in Figures 6(b) and 6(c) show the wake at phase angles $\phi = 0$ and π, showing spanwise symmetry in both the u_{ROM} contours and the streamlines. At $\phi = 0$, the streamlines show two pairs of counter-rotating vortices, the first at [y/H, z/H] = [-0.24, 0.16] and [0.24, 0.16], and the second at [y/H, z/H] = [-0.12, -0.31] and [0.12, -0.31]. As the phase angle increases to $\phi = \pi$, the upper pair of vortices move towards [y/H, z/H] = [-0.46, -0.07] and [0.46, -0.07] while the lower vortices move in the spanwise direction towards y/H = 0 and disappear. In the remaining phase from $\phi = \pi$ to 2π, the upper vortices are no longer present.

The small vertical motion of the barycentre and symmetry-preserving SPOD mode are consistent with the observations of Chen et al. (2024) at a similar St range, labelled as vertical flapping motions. Vertical flapping motions form the first mode in zone III and the second mode in zone II. Contrary to these findings, Chen et al. (2024) did not report distinct St ranges for

the vertical and spanwise flapping motions, nor was a significant energy peak found for swinging/flapping motions at low *Re*.

Vortex Shedding

This section discusses the SPOD modes in the range of $0.110 \leq St < 0.250$, or zone IV in Figure 3. Figure 7(a) shows a trace of the barycentre for the first mode at $Re = 232{,}000$ at $St = 0.149$, consistent with the first energy peak in this zone. The barycentre oscillates in the spanwise direction over one full cycle from $y/H = -0.04$ to 0.03, similar to the spanwise flapping motions described above. In Figure 7(b), the reconstruction of the ROM at phase $\phi = 0$, there is one dominant streamwise vortex centered at $[y/H, z/H] = [0.39, -0.12]$. As the phase angle increases from $\phi = 0$ to $\pi/2$, the vortex moves in the spanwise direction towards the spanwise center and disappears. From $\phi = \pi/2$ to π, the vortex reappears and is centered at $[y/H, z/H] = [-0.39, -0.12]$.

The second peak in this zone occurs at a frequency of $St = 0.195$ as shown in Figure 7(d-f). The barycentre trace shows a wall-normal switching of the barycentre location concentrated near the bottom of the Ahmed body for most of the motion. Interestingly, unlike the spanwise vortex shedding pattern, characteristic of this motion are two counter-rotating vortices near the spanwise centre of the Ahmed body that oscillate in the wall-normal direction. Additionally, wall-normal vortex shedding shows a larger wall-normal displacement of the barycentre compared to vertical flapping motions.

Other Flow Motions

Zone V in Figure 3 is representative of small-scale turbulent structures that are not coherent. The high *Re* measurements do not show final peak present in low *Re* as shown in Figure 2, which represents shear layer instability. This is likely due to the smaller upper limit of the *St* numbers measured at high *Re*. It was decided to measure at a lower *St* range to better capture bi-stability motions, at the expense of possible shear layer instability motions at higher *St*.

CONCLUSIONS

The investigation into the wake dynamics of the Ahmed body showed consistency between analyses carried out using full 3D measurement and a crossflow slice of the same data for energy distribution at different *St* and traces of the barycentre. Based on this evaluation, 2D crossflow measurements can be used to distinguish patterns in the wake dynamics for different *St* ranges. Using stereo-PIV measurements at high *Re* and analysis using SPOD, five distinct flow motions were observed. New peaks in the energy of the first SPOD mode emerge at *St* corresponding to vertical flapping and spanwise vortex shedding for higher *Re*. New *St* ranges for spanwise and vertical flapping were introduced to distinguish the frequencies of the two motions. At $St < 0.016$, bi-stability motions were observed, characteristic of which were large spanwise displacements of the barycentre, as well as two counter-rotating vortices. Between *St* of 0.016 and 0.051, spanwise flapping motions were observed, which were comprised of smaller spanwise oscillations of the barycentre, as well as two weaker vortices. Vertical flapping motions were found between *St* of 0.051 and 0.110, characteristic of which is a vertical motion of the barycentre. Two energy peaks within the *St* range of 0.110 and 0.250 were representative of spanwise and wall-normal vortex shedding, respectively. The observed motions are consistent with those found at low *Re*, with greater resolution of bi-stability and vertical/spanwise flapping motions. Finally, shear layer instability was not observed at high *Re*, possibly due to a smaller chosen *St* upper limit.

REFERENCES

Ahmed, S. R., Ramm, G., and Faltin, G., 1984, "Some Salient Features of the Time -Averaged Ground Vehicle Wake", *SAE Transactions*, SAE International, Vol. 93, pp. 473–503.

Chen, C. W., Wang, S., and Ghaemi, S., 2024, "Spectral proper orthogonal decomposition of time-resolved three-dimensional flow measurements in the turbulent wake of the Ahmed body", *Journal of Fluid Mechanics*, Vol. 985, p. A19.

Duell, E. G. and George, A. R., 1999, "Experimental Study of a Ground Vehicle Body Unsteady Near Wake", *SAE Transactions*, SAE International, Vol. 108, pp. 1589–1602.

Grandemange, M., Gohlke, M., and Cadot, O., 2013, "Turbulent wake past a three-dimensional blunt body Part 1 Global modes and bi-stability", *Journal of Fluid Mechanics*, Vol. 722, pp. 51–84.

Haffner, Y., Borée, J., Spohn, A., and Castelain, T., 2020, "Mechanics of bluff body drag reduction during transient near-wake reversals", *Journal of Fluid Mechanics*, Vol. 894, p. A14.

Hanson, R. E., Buckley, H. P., and Lavoie, P., 2012, "Aerodynamic optimization of the flat-plate leading edge for experimental studies of laminar and transitional boundary layers", *Experiments in Fluids*, Vol. 53, pp. 863–71.

Khalighi, B., Zhang, S., Koromilas, C., Balkanyi, S. R., Bernal, L. P., Iaccarino, G., and Moin, P., 2001, "Experimental and Computational Study of Unsteady Wake Flow Behind a Bluff Body with a Drag Reduction Device", *SAE Transactions*, SAE International, Vol. 110, pp. 1209–22.

Nekkanti, A. and Schmidt, O. T., 2021, "Frequency–time analysis, low-rank reconstruction and denoising of turbulent flows using SPOD", *Journal of Fluid Mechanics*, Vol. 926, p. A26.

Pavia, G., Passmore, M., and Sardu, C., 2018, "Evolution of the bi-stable wake of a square-back automotive shape", *Experiments in Fluids*, Vol. 59, p. 20.

Podvin, B., Pellerin, S., Fraigneau, Y., Evrard, A., and Cadot, O., 2020, "Proper orthogonal decomposition analysis and modelling of the wake deviation behind a squareback Ahmed body", *Physical Review Fluids*, Vol. 5, p. 064612.

Prasad, A. K. and Jensen, K., 1995, "Scheimpflug stereocamera for particle image velocimetry in liquid flows", *Applied Optics*, Vol. 34, p. 7092.

Sirovich, L., 1987, "Turbulence and the dynamics of coherent structures II Symmetries and transformations", *Quarterly of Applied Mathematics*, Vol. 45, pp. 573–82.

Towne, A., Schmidt, O. T., and Colonius, T., 2018, "Spectral proper orthogonal decomposition and its relationship to dynamic mode decomposition and resolvent analysis", *Journal of Fluid Mechanics*, Vol. 847, pp. 821–67.

Westerweel, J. and Scarano, F., 2005, "Universal outlier detection for PIV data", *Experiments in Fluids*, Vol. 39, pp. 1096–1100.